Comprehensive mobility study of silicon nanowire transistors using multi-subband models

NANO EXPRESS

PAPER

Comprehensive mobility study of silicon nanowire transistors using multi-subband models

Cristina Medina-Bailon[1,2,*], **Mihail Nedjalkov**[3], **Vihar Georgiev**[1], **Siegfried Selberherr**[3] **and Asen Asenov**[1]

[1] Device Modelling Group, School of Engineering, University of Glasgow, Glasgow G12 8LT, Scotland, United Kingdom
[2] Nanoelectronics Research Group, Departamento de Electrónica y Tecnología de Computadores, Universidad de Granada, 18071 Granada, Spain
[3] Institute for Microelectronics, TU Wien, Gußhausstraß27-29/E360, 1040 Wien, Austria
[*] Author to whom any correspondence should be addressed.

E-mail: cmedba@ugr.es **and** vihar.georgiev@glasgow.ac.uk

Keywords: silicon nanowire field-effect transistors, one-dimensional multi-subband scattering models, confined charge transport, Poisson-Schroödinger solvers, Kubo-Greenwood formalism

OPEN ACCESS

RECEIVED
22 March 2023

REVISED
15 May 2023

ACCEPTED FOR PUBLICATION
5 June 2023

PUBLISHED
20 June 2023

Abstract

Spatial confinement is important in advanced More Moore devices, such as nanowire transistors (NWTs), where the basic charge transport properties must be revised beyond the bulk crystal assumptions. This work presents a comprehensive and general overview of the electron mobility in aggressively-scaled Si NWTs in order to demonstrate the effect of quantum confinement on this topic, establishing its dependence on numerous physical factors (shape, diameter, and orientation). The mobility evaluation makes use of a unique simulation framework and innovative multi-subband calculations of the scattering rates. We show that (1) the effect of surface roughness scattering is more pronounced at higher sheet densities, (2) ionized impurity scattering seriously degrades the mobility in highly-doped NWTs, and (3) the cross-section shape affects directly the subband parameters and the mobility, with the elliptical NWTs giving the best performance for the same cross-sectional area.

1. Introduction

For several years now, the scaling limit of conventional CMOS technology has been a hot topic of discussion. To maintain progress in semiconductor electronics beyond such a limit, various device technologies are investigated aiming for an extension of the end of the technology roadmap. Several device solutions have been floated as possible candidates, including tunnel field effect transistors (TFETs) [1–3] and multiple gate structures [e.g. FinFETs] [4]. Within this dynamic context of nanoscale device development, gate-all-around (GAA) nanowire transistors (NWTs) are gaining considerable interest [5–11], as an extension of the FinFET CMOS technology to the ultimate scaling limit. Advantages of GAA NWTs are numerous, for instance: minimized short channel effects or the possibility of using strain and material engineering to improve device performance.

Considering the importance of spatial confinement in advanced More Moore devices, the charge transport properties derived under the bulk crystal assumption must be revised. At such small device sizes, one cannot rely on the Bloch theorem, since mobile carriers are confined in the cross-section normal to the transport direction. In such low-dimensional structures, the carriers must not be treated as point-like particles (whose motion is constrained in the confinement plane), energy is quantized into subbands, the momentum of a localized carrier is not well defined, and the momentum conservation is only valid in the transport direction. In this context, transport simulation approaches incorporating quantum effects into semi-classical models [12–14] have become popular, because of their lower computational demand compared to rigorous quantum transport models [15–17]. Si NWTs cease to have a bulk-like electronic structure for diameters smaller than 8 nm, at which transport is governed by multisubband scattering [5], whose rates are modified by the overlap factor of the subbands involved in the carrier transition events [18]. Accordingly, any realistic transport model must accurately reproduce the experimental energy gaps and effective masses for the most relevant subbands.

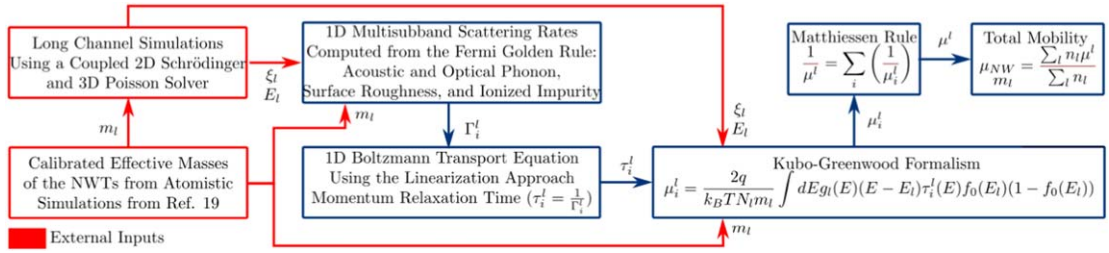

Figure 1. Illustration of the simulation flowchart and the corresponding steps needed to calculate the total mobility. l is the subband index; m_l, ξ_l, and E_l are the calibrated effective masses, the wavefunction, and the energy level for the l^{th} subband, respectively; i is the i^{th} scattering mechanism; τ_i^l, Γ_i^l, and μ_i^l are the relaxation time, scattering rate, and mobility, respectively, for the i^{th} mechanism and the l^{th} subband; μ_{NW} is the total mobility for a particular NWT structure.

Considerable work has been carried out to evaluate the mobility of Si NWTs, relying mainly on the Kubo-Greenwood (KG) formalism [12–14], and to a lesser extent on Monte Carlo and other one-dimensional (1D) Boltzmann equation solvers [5], and atomistic simulation methods [15–17]. However, more work is needed, not only to evaluate the performance of NWTs with Si and alternative material channels, but also to propose optimal device designs at the scaling limit. The main objective of this work is two-fold: 1) we provide a comprehensive and general overview of the electron mobility in aggressively-scaled Si NWTs making a systematic study of the important effects, mainly the scattering mechanisms, diameter, cross-sectional shape, and orientation; and 2) the simulation framework combines a unique combination of sophisticated simulation solvers, first principle calculation of material properties, and complex physical models for the quantum process.

This paper is organized as follows. In section 2, the modeling approach, including the mobility simulation framework and considered formalisms, is presented. Section 2 is complemented by appendix, where the innovative derivations and scattering rates are listed. In section 3, we carry out a systematic analysis of mobility dependence on the most important physical factors. Finally, we summarize the main findings in section 4.

2. Simulation framework

The approach herein considered is based on the long-channel simulation model [10, 11]. This framework provides reliable mobility values at low-field near-equilibrium conditions in devices with strong confinement effects, such as NWTs. The simulation process (figure 1) involves applying the following four-step strategy.

First, the confinement and transport effective masses (m_{eff}) are evaluated beforehand from first principles simulations, accounting for the impact of the cross-section diameters and shapes of the nanowires. They are calibrated with the sp3d5s* tight-binding model using a Boykin parameter set, as discussed in [19]. The calculations were implemented using the QuantumATK package from Synopsys [20].

Second, we employ the coupled three-dimensional (3D) Poisson—two-dimensional (2D) Schrödinger solver integrated within the TCAD simulator GARAND from Synopsys [21] to calculate the potential distribution, the electron concentration, and the subband details of the long channel gated NWT. The 1D Boltzmann transport equation (BTE) must be solved in conjunction with other equations, such as the Poisson and Schrödinger equations. Intensive computations are involved in the evaluation of the multisubband energies and the eigenfunctions, and the self-consistent potential distribution in the wire, which implies that numerical aspects are an important factor for the feasibility of the given refined model. Its establishment is thus a matter of compromise between physical accuracy and numerical efficiency. As shown in figure 2, we couple the 2D solution of the Schrödinger equation in multiple slices (i.e. the cross-section areas of the long channel) to a 3D Poisson solution in the structure based on a Si GAA NWT. This step provides useful quantities including the electric potential and field distribution (used for surface roughness scattering), the details of the subbands (eigenfunctions and eigenvalues) and subband electron concentrations (needed for all scattering processes and KG mobility calculations). It is important to highlight that, despite the fact that this description is not as accurate as the one that could be obtained employing multiple-band k·p or atomistic models to describe the electronic band structure, it can provide reliable results [22, 23] with correctly fitted values of the effective masses for Si nanowires below a diameter of 5 nm (as t is described in the previous step).

Third, we use the above-mentioned parameters to calculate the corresponding 1D rates for the dominant scattering mechanisms. We implement models for the electron interaction mechanisms with both acoustic (Ac-Ph) and optical (Op-Ph) phonons and ionized impurities (II), which are considered as high and low field mobility limiting mechanisms, respectively. We also include surface roughness (SR), as it can play an important role at high charge densities and in nanostructures where confinement keeps the electrons close to non-ideal

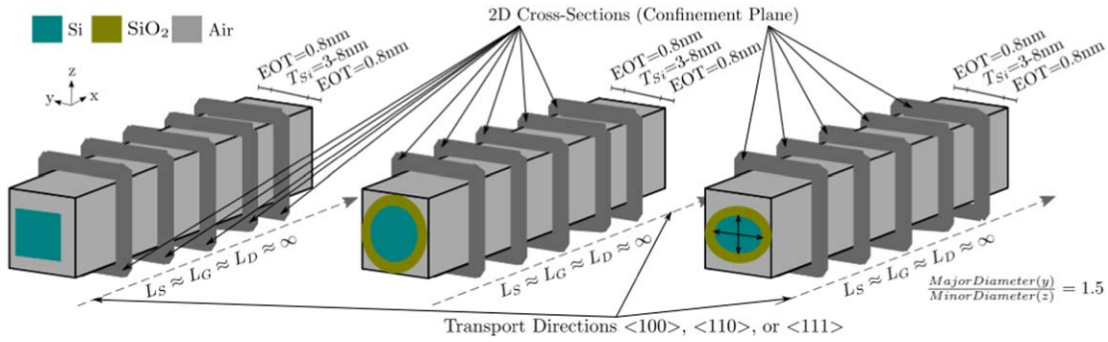

Figure 2. Schematic illustration of *Si* Square, Circular, and Elliptic NWTs with widths (T_{Si}) ranging from 3 nm to 8 nm and a fixed SiO_2 Equivalent Oxide Thickness (EOT = 0.8 nm). Three different transport directions have been herein evaluated. The coupled 3D Poisson and 2D Schrödinger equations are solved for each cross-section and then the scattering rates are calculated for each subband.

interfaces. In this work, the calculations are performed within the ellipsoidal non-parabolic bandstructure valley approximation. Appendix provides a full description of the derivation of every individual scattering mechanism.

Forth, we use the semi-classical BTE in the relaxation time approximation adopting the KG formalism to calculate the mobilities of the NWTs. The developed mobility model involves the multi-subband scattering mechanisms discussed above and the application of the KG theory to confined 1D electron gases. The semi-classical study of the transport properties of a 1D electron gas implies the solution of the BTE, which is not straightforward in complex structures. In our approach, the evaluation of the electron mobility using the KG formula, and involving the relaxation times, are obtained with the solution of the linearized BTE. This mobility theory involves a set of approximations used to define the momentum relaxation time of the 1D electron gas. The mobility calculations for a subband (l) are carried out in two stages (figure 1): the mobility (μ_i^l) associated with each particular scattering mechanism (i) is calculated using its rate (Γ_i^l) by applying the KG formula; and, then, the total mobility (μ^l) is calculated as a function of the individual ones using the Matthiessen rule [24].

It is worth mentioning here that, during the development of this code, we validated our models with published trends [25, 26] in order to show their accuracy in comparison to more complex approaches and to choose the adequate scattering parameters for each mechanism. This calibration is not shown here as it is out-of-scope of this paper.

3. Results and discussion

Unless stated otherwise, the results below are presented for square NWTs with a typical line density of 2.7×10^6 cm^{-1} and [110] orientation. The main reason of this chosen moderately high line density is to avoid the individual dominance of the surface roughness scattering mechanism over the phonon or ionized impurity mechanisms at high carrier concentrations [26]. The impact of the shape, width, and orientation are specifically stated in some figures (figure 1 illustrates the simulated NWTs and lists these device parameters and the corresponding fixed ones). For SR scattering, typical values [26] for the root mean square of the variance ($\Delta_{RMS} = 0.48$ nm) and the correlation length ($\lambda = 1.3$ nm) have been chosen. For II scattering, a non-really high fixed II concentration of $N_I = 10^{18}$ cm^{-3} is assumed [10, 25]. The total number of subbands for each conduction band valley is twenty.

The KG formalism has the advantage of allowing the analysis of the individual impact of each scattering mechanism on the overall nanostructure mobility which decreases with the increasing scattering rate. Figure 3 shows the rates for Ac-Ph, Op-Ph (including g-type and f-type transitions), SR, and II scatterings, as a function of the total energy, for 3 nm (figures 3(a)–(c)), 5 nm (figures 3(d)–(f)), and 8 nm (figures 3(g)–(i)) diameter square NWTs. Several conclusions can be highlighted if this figure is analyzed focusing on the impact of the diameter or each mechanism individually. First, the multisubband effects in the scattering rates are more pronounced for smaller nanowire width. This is associated with the higher energy difference among subbands, which minimizes the possible electron transitions between subbands. This can be shown in the figures with the scattering rates as each different peak represents a subband energy: these peaks are more pronounced and separated for the smallest case (figures 3(a)–(b)), whereas they are lower and nearby for the for biggest one (figures 3(g)–(h)). In the latter, it is even possible to distinguish that there are no subbands (peaks) after a total energy of 0.6 eV. Second, keeping in mind that, at low fields, most electrons are located at the lowest subbands (< few k_BTs), Ac-Ph scattering is expected to be the main limiting mobility factor in comparison to other phonon mechanisms independently of the diameter, as depicted in figures 3(a), (d), and (g). Third, as suggested by figures 3(b), (e), and (h), the effect of II scattering will dominate in structures with a high level of ionized impurities as indicated by its comparatively high rate at low energies in

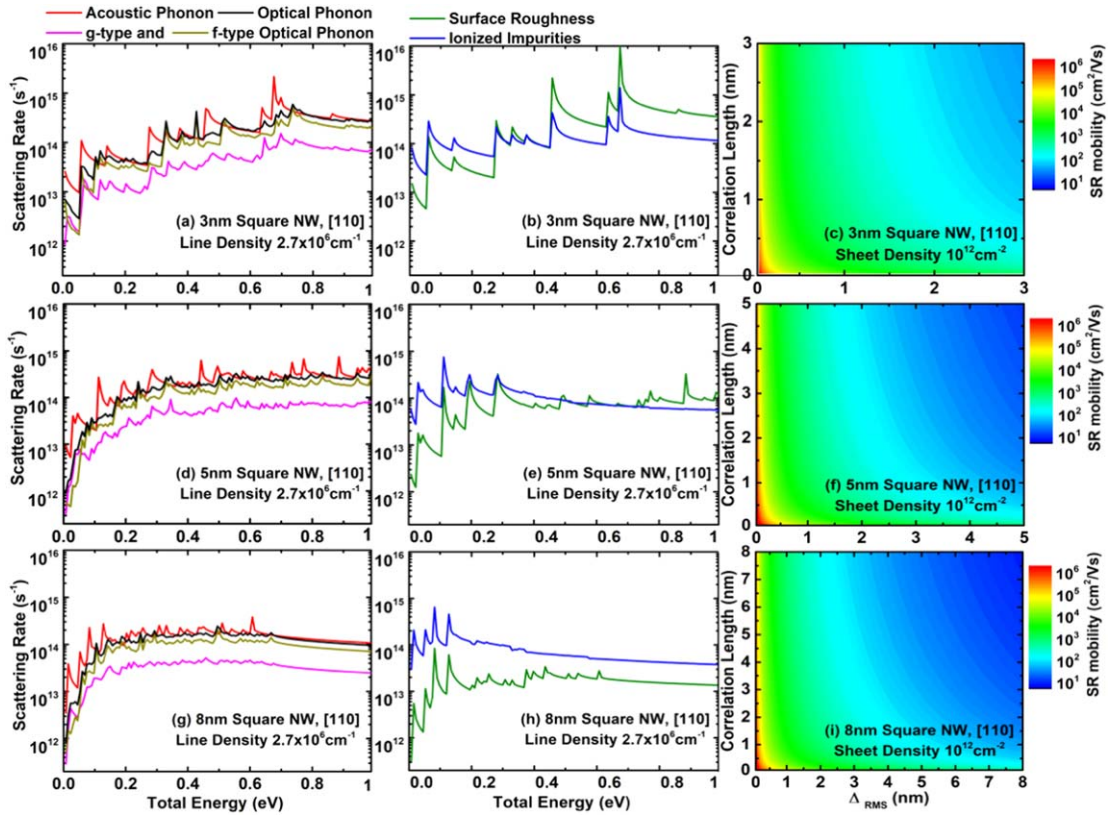

Figure 3. The rates for (a)/(d)/(g) acoustic and optical phonons, including g-type and f-type transitions, and (b)/(e)/(h) surface roughness and ionized impurity scatterings as a function of the total energy. (c)/(f)/(i) Surface roughness limited mobility as a function of the SR parameters: root mean square (Δ_{RMS}) and correlation length. The results are for (a)–(c) 3 nm, (d)–(f) 5 nm, and (g)–(i) 8 nm square NWTs, [110] orientation, and a line density of 2.7×10^6 cm^{-1}.

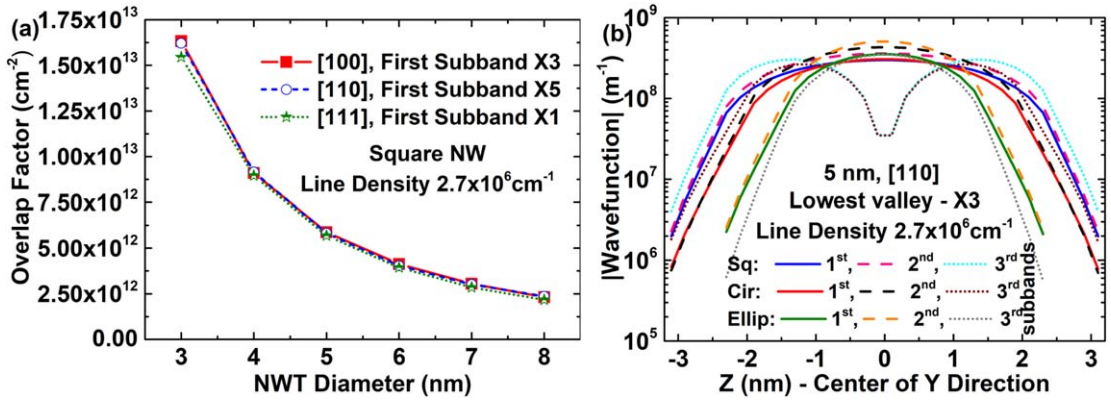

Figure 4. (a) Overlap factor for the square NWT as a function of the diameter with [100], [110], and [110] orientations, being calculated for the fundamental subband (1st subband of valley X3, X5, and X1, respectively,) and intra-valley transitions. (b) Wavefunction modulus of the three first subbands of the lowest valley (X3) for square, circular, and elliptic NW structures considering the 5 nm diameter and [110] orientation. The line density is 2.7×10^6 cm^{-1} in both figures.

comparison to the SR scattering for the three widths. Fourth, the adverse effect of SR, also shown in figures 3(b), (e), and (h), is expected to be more pronounced as the total energy increases and the device width decreases. Specifically from around 0.5 eV, this rate is much higher, roughly similar, and much slower in comparison to the II rate in the 3 nm (figure 3(b)), 5 nm (figure 3(e)), and 8 nm (figure 3(h)) cases, respectively. Finally, it is worth emphasizing that the impact of SR scattering strongly depends on fabrication technology, which we try to capture via Δ_{RMS} and λ. This is illustrated in figures 3(c), (f), and (i), showing the SR limited mobility as a function of both parameters for the same device than in figures 3(a)–(b), (d)–(e), and (g)–(h), respectively. As it can be seen, there exists roughly an exponential dependence of such mobility with both parameters, although such dependence is much stronger when varying Δ_{RMS}.

The overlap factors and subband levels are equally important when determining the mobilities, considering their impact on the scattering rates. Figure 4(a) shows example overlap factors for the square nanowire, as a

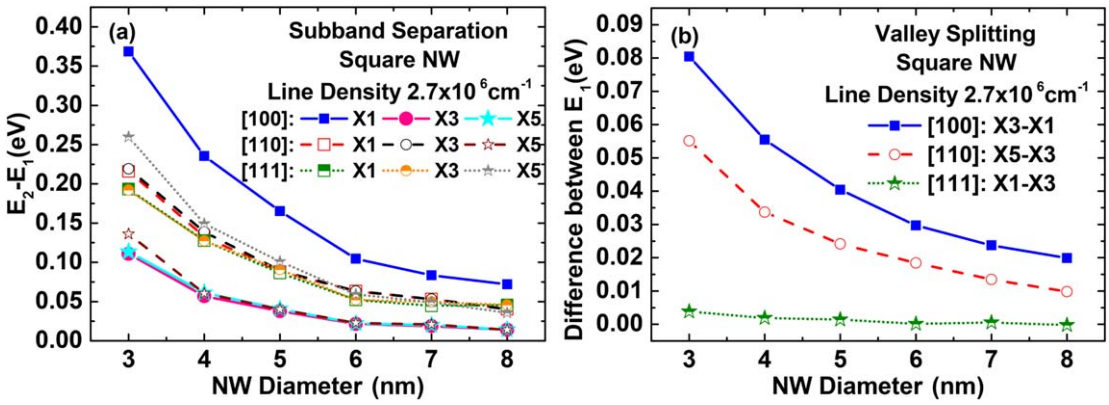

Figure 5. Subband differences depicted as a function of the diameter for square NWTs with [100], [110], and [110] orientations and a line density of 2.7 $\times$ 10^6 cm^{-1}: (a) between the 1st and the 2nd energy subband levels; and (b) between the smallest and the largest 1st subband energies among the delta valleys.

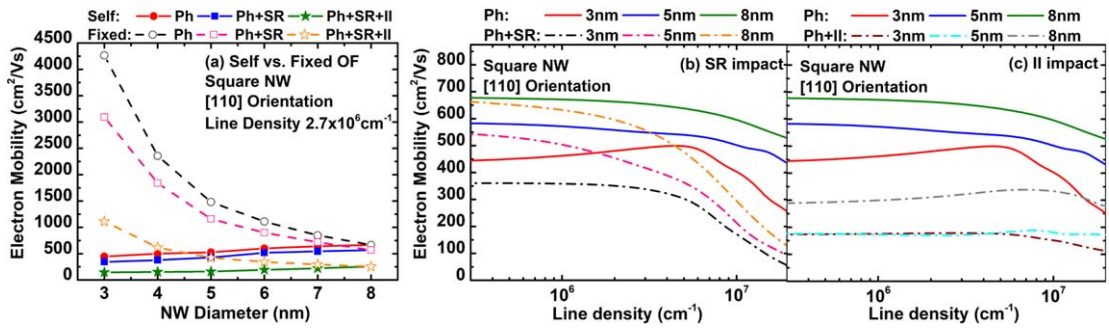

Figure 6. Electron mobility for square NWT with [110] channel orientation considering the impact of total phonon (Ph), surface roughness (SR), ionized impurity (II) scattering mechanisms as well as different combinations of them: (a) Electron Mobility as a function of the diameter considering self-consistent (Self) and fixed (Fixed) overlap factors with a line density of 2.7 $\times$ 10^6 cm^{-1}; and (b)–(c) Electron Mobility as a function of the line density for 3 nm, 5 nm, and 8 nm diameters accounting for the impact of Ph, (b) Ph+SR, and (c) Ph+II.

function of the diameter for [100], [110], and [110] transport directions, calculated for the fundamental subband (1st subband of valleys X3, X5, and X1, respectively) and intra-valley transitions. The overlap factor is an integral, over the cross-sectional area along the confinement directions normal to the 1D transport direction, of the wavefunction in the 1st subband multiplied by the wavefunction in the final valley. The observed increase in the overlap factor at smaller diameters is a direct result of modifying the population and wavefunction features of different subbands in smaller cross-sections. Since the scattering rates are directly proportional to the overlap factor, they generally increase as the diameter (cross-section area) is reduced resulting in smaller electron mobilities. While figure 4(a) presents the case for a square NWT, the trend applies for any other cross-section shape. Indeed, since the NWT area is the main factor determining the overlap factor, this quantity is almost identical for different NWT shapes at the same area [11]. An example is shown in figure 4(b), where the wavefunction modulus of the three 1st subbands of the lowest valley (X3) for square, circular, and elliptic NWTs considering the 5 nm diameter and [110] channel orientation is shown. It graphically illustrates that for the same diameter, as the area for each shape is different, the equivalent wavefunctions are different.

Figure 5(a) shows the difference between the 1st and the 2nd energy subband levels, while figure 5(b) shows the difference between the smallest and the largest first subband energies among the delta valleys, all for the square NWT as a function of the diameter and for [100], [110], and [110] transport directions. Both parameters are consequential, since a larger separation between two subbands (two valleys) imply a lower impact of inter-subband (inter-valley) scattering on mobility. However, since a smaller valley separation implies a more distributed population in various valleys, the mobility can increase in the case where the lowest subband has a higher transport effective mass. As can be seen, the energy separations increase as the diameter decreases, and at very small diameters transport takes place exclusively at the lowest subband of the lowest valley. Figure 5(a) shows that this subband separation considering the lowest valley for [100] (X3) and [110] (X5) are almost the same, but are lower than that obtained for a [111] orientation (X1). Nevertheless, this possible advantage is countered by the much higher inter-valley separation in both [100] and [110] orientations.

Figure 6(a) shows the electron mobility as a function of the nanowire cross-section area, accounting for the impact of (i) Ph scattering, (ii) Ph+SR scatterings, and (iii) Ph+SR+II scatterings. Here, the results present two

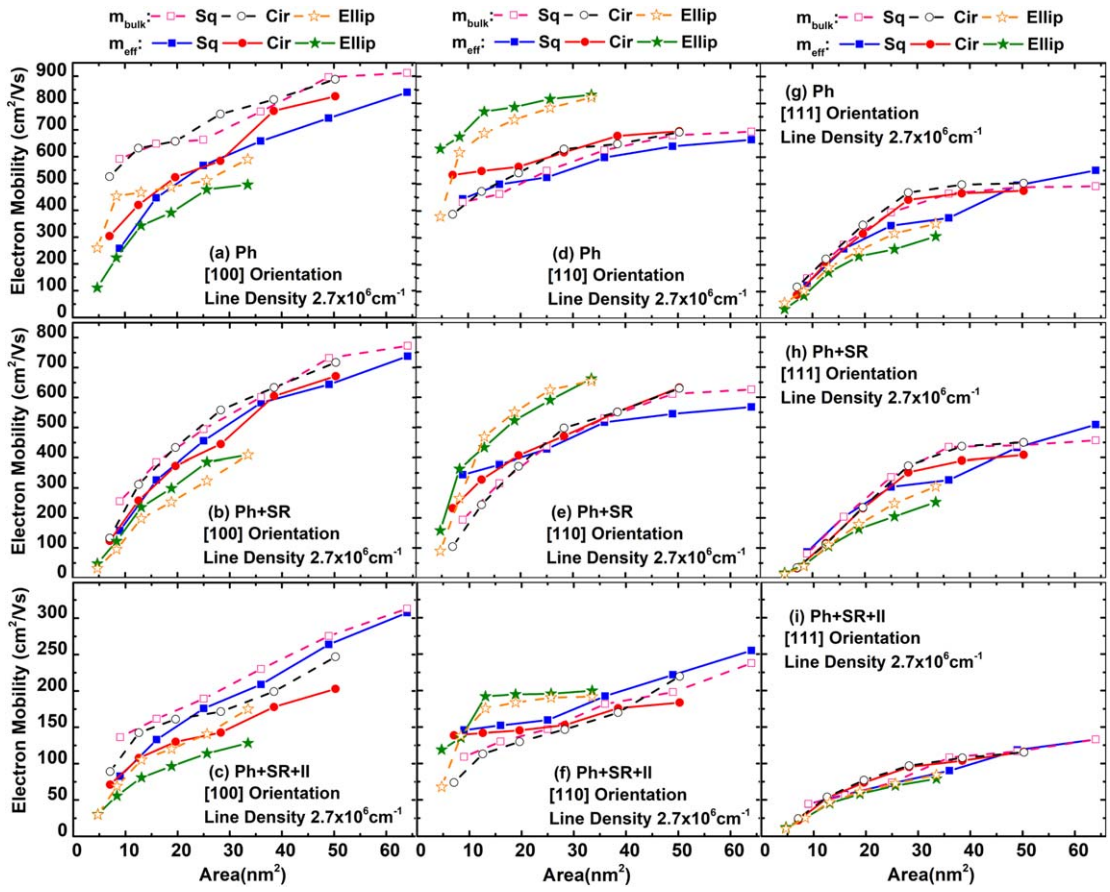

Figure 7. Electron Mobility as a function of the area considering the impact of phonon scattering ((a), (d), and (g)), phonon and surface roughness scatterings ((b), (e), and (h)), and phonon, surface roughness and impurity scattering ((c), (f), and (i)) for square, circular and elliptic NWTs with the calculated (m_{eff}) and bulk (m_{bulk}) effective masses. The results are for (a)–(c) [100], (d)–(f) [110], and (g)-(i) [111] channel orientations and a line density of 2.7×10^6 cm^{-1}.

types of curves. The first type uses the correct overlap factor which is computed self-consistently, whereas the second type uses a constant overlap factor which is chosen conveniently (set to the value at the highest diameter considered) to highlight its quantitative and qualitative impact. It is noteworthy that the application of a fixed overlap factor is for illustrative purposes only. Indeed, figure 6(a) highlights the significant effect of the overlap factor on mobility, especially at lower diameters. The self-consistent (correct) mobility results confirm our earlier conclusions about how Ph scattering mechanisms have a dominant effect on transport in undoped nanowires. They also confirm the disadvantage of using doped nanowires, as II scattering reduces the mobilities significantly.

Figures 6(b)–(c) illustrates the impact of SR and II scatterings, by showing the electron mobility as a function of the line density, considering only Ph scattering and the combined effect of Ph+SR (figure 6(b)) and Ph+II (figure 6(c)) scatterings, for a square NWT with various diameters. In general, the mobility falls down as the diameters are shrunk, due to the increasing scattering rates. As expected from the KG formulation, the mobility also typically falls down at very high carrier concentrations. This is especially true when including SR scattering, due to the increased scattering rates resulting from higher cross-sectional electric field magnitudes, in agreement with published data [14, 16, 26, 27]. Not surprisingly, for the same diameter, the impact of SR scattering is modest to moderate at low carrier concentrations to dramatic at high densities, resulting in roughly a fourfold reduction in mobility at a line density of 2×10^7 cm^{-1}. On the other side, by including II scattering in a nanowire incorporating a moderately high concentration of ionized impurities ($N_I = 10^{18} cm^{-3}$ in this case), we obtain expectedly a dramatic reduction in the total mobility. Interestingly, however, the mobility itself remains almost unchanged. This observation can be interpreted as an advantage for devices operating at high densities, but this also indicates the dominance and (hence the adverse effect) of II scattering on electron transport in NWTs, being the total mobility is still much lower than the photon limited mobility.

Figure 7 shows the electron mobility as a function of the cross-section area, considering the impact of (i) Ph scattering, the combined impact of (ii) Ph+SR scatterings and (iii) Ph+SR+II scatterings, with two sets of curves using either m_{eff} or the bulk effective masses (m_{bulk}). The results are for square, circular and elliptic NWTs

and [100], [110], and [111] orientations. It is noteworthy that the results considering m_{bulk} are for illustrative purposes only as neglecting m_{eff} leads to unreliable higher mobility, especially at low diameters. The mobility is underestimated by 50% at the lowest diameter considered for the elliptical case. Most importantly, we observe that, for the same cross-section area, elliptical NWTs provide the highest mobilities for the same area, although this advantage is visibly minimized in structures incorporating high ionized impurity concentrations. In the case where both SR and II are negligible, circular NWTs seem to perform better than square ones. With the presence of SR scattering, the performance of circular NWTs is degraded at lower diameters, making square NWTs better for areas (diameters) below 25 nm^2 (5 nm). With a strong of SR and II scattering, square NWTs seem to outperform circular ones at all the diameters considered.

These qualitative conclusions are specifically made for a [110] channel orientation, but they apply also to the other two orientations, being clear that the [111] one provides the worst performance. It can also be seen that [100] orientation performs better at low diameters while the [110] one performs better at larger diameters. The difference in the mobilities of various cross-section shapes is due to a complex combination of effects which may enhance or degrade performance, such as subband and valley splitting energies, the electrostatic characteristics, and the overlap factor obtained from the solution of the Schrödinger equation. An example illustration was shown in figure 4(b). It graphically illustrates e.g. how for the same diameter (5 nm), the wavefunctions (and so the overlap factors) can vary wildly, affecting the scattering rates, and hence the mobility differently.

4. Conclusion

By using a unique 1D multi-subband simulation model, we present a complete study of electron mobility in Si NWTs with various sizes, cross-section shapes, and orientations. In addition to highlighting the impact of the relevant scattering mechanisms, we emphasize the importance of using multi-subband models, accounting correctly for quantum confinement over the bulk device simulations. We can draw several interesting conclusions from our calculations. First, acoustic phonon scattering is the dominating factor when determining the low-carrier concentration mobilities, although at high fields optical phonons also start to play a tangible role. Second, surface roughness scattering has a visible detrimental effect on mobility, and its impact starts to dominate at high carrier concentrations. Third, whereas the presence of ionized impurities in quantum wire channels is undesirable, their presence by a high concentration can have a significantly detrimental effect on the mobility. Fourth, elliptical NWTs provide the highest mobilities for the same cross section area, although such an advantage is almost quashed in the presence of high ionized impurity concentrations.

Acknowledgments

The research leading to these results has received funding from the European Union's Horizon 2020 research and innovation programme under grant agreement No 688 101 SUPERAID7 and by Juan de la Cierva Incorporación Fellowship scheme under grant agreement No. IJC2019-040003-I (MICINN/AEI). Moreover, the coauthors would like to thank Dr. Sadi, Dr. Towie, Dr. Lee, and Dr. Donetti for useful discussions.

Data availability statement

The data cannot be made publicly available upon publication because they are not available in a format that is sufficiently accessible or reusable by other researchers. The data that support the findings of this study are available upon reasonable request from the authors.

Appendix. Scattering rates derivations

A.1. Acoustic phonon scattering rate derivation

We include acoustic phonon scattering mechanisms in the elastic parabolic equipartition approximation, within the short wave vector limit [28]. After extensive derivations, the scattering rate is given by

$$\Gamma_{ac,l,k} = \frac{|D_{ac}|^2 k_B T}{\rho \hbar \bar{u}^2} \frac{m}{\hbar^2} \sum_{l'} \left[\int d\mathbf{s} |\xi_l(\mathbf{s})|^2 |\xi_{l'}(\mathbf{s})|^2 \right] \times \theta(\epsilon(k) + \Delta E_{l'}) \left(\frac{1}{|q_2 + k|} + \frac{1}{|q_1 + k|} \right) \tag{A1}$$

with

$$q_{1,2} = -k \pm \sqrt{k^2 + \frac{(E_l - E_{l'})2m}{\hbar^2}}. \tag{A2}$$

D_{ac} is the deformation potential, k_B is the Boltzmann constant, T is the lattice temperature, ρ is the material density, $\hbar$ is the reduced Planck's constant, $\bar{u}$ is the speed of sound, and m is the electron effective mass. l and l' refer to the initial and final electron subbands, $\mathbf{s}$ is the vector normal to the transport direction, ξ are the wavefunctions at the given subband, θ represents the heaviside step function, $\epsilon(k)$ is the kinetic energy for a wavevector magnitude k, and $\Delta E_{l'} = E_{l'} - E_l$ is the energy separation between subbands l and l'.

A.2. Optical phonon scattering rate derivation

The energies of the different branches of deformation potential optical phonons $\hbar\omega_j(\mathbf{q}) = \hbar\omega_j$ (short wavevector limit $|\mathbf{q}| \to 0$) are approximated with constants, as it is standard. Accordingly, the equilibrium phonon number is wavevector ($\mathbf{q}$) independent, so that the expression for the scattering rate depends on the two factors n_j and $(n_j + 1)$. The scattering rate can be written as

$$\Gamma_{op,j,l,k} = \sum_{l'} \int dk' S(op, j, l, k \to l', k'), \tag{A3}$$

where S is the scattering probability. By using the definitions

$$\Delta E^{+}_{l'j} = E_l - E_{l'} + \hbar\omega_j, \qquad \Delta E^{-}_{l'j} = E_l - E_{l'} - \hbar\omega_j \tag{A4}$$

the rate can be rewritten as

$$\Gamma_{op,j,l,k} = \frac{|D_{op,j}|^2}{2\rho\omega_j} \sum_{l'} \left[\int d\mathbf{s} |\xi_l(\mathbf{s})|^2 |\xi_{l'}(\mathbf{s})|^2 \right] \int dq G(q), \tag{A5}$$

where

$$\begin{aligned} \int dq G(q) = {} & \frac{n_j \theta(\epsilon(k) + \Delta E^{+}_{l'j}) m_{v'}}{\hbar^2} \left(\frac{1}{|q_1 + k|} + \frac{1}{|q_2 + k|} \right) \\ & + \frac{(n_j + 1)\theta(\epsilon(k) + \Delta E^{-}_{l'j}) m_{v'}}{\hbar^2} \left(\frac{1}{|q_3 + k|} + \frac{1}{|q_4 + k|} \right) \end{aligned} \tag{A6}$$

with

$$q_{1,2} = -k \pm \sqrt{\frac{m_{v'}}{m_v} k^2 + \frac{(E_l + \hbar\omega_j - E_{l'})2m_{v'}}{\hbar^2}} \tag{A7}$$

and

$$q_{3,4} = -k \pm \sqrt{\frac{m_{v'}}{m_v} k^2 + \frac{(E_l - \hbar\omega_j - E_{l'})2m_{v'}}{\hbar^2}}. \tag{A8}$$

j refers to the phonon mode, ω_j is the phonon energy, and m_v ($m_{v'}$) are the transport effective masses of the initial (final) valley, for the inter-valley transitions.

A.3. Ionized impurity scattering rate derivation

The screened Coulomb potential of an impurity at $(\mathbf{S}, 0)$ and an electron at $(\mathbf{s}, z)$ [25] is

$$V(\mathbf{r}) = \frac{Z_I e^2}{4\pi\epsilon\sqrt{(\mathbf{S} - \mathbf{s})^2 + z^2}} e^{-(\sqrt{(\mathbf{S}-\mathbf{s})^2 + z^2})/L_D}, \tag{A9}$$

where, for a multi-subband case, the screening (Debye) length L_D is given by

$$L_D^2 = \frac{kT\epsilon}{e^2 n_0} \frac{\sum_l \mathcal{F}_{-1/2}((E_l - E_F)/kT)}{\sum_l \mathcal{F}_{-3/2}((E_l - E_F)/kT)}, \tag{A10}$$

where $\mathcal{F}_n$ is the Fermi integral of order n, and n_0 is the equilibrium electron concentration. The scattering rate is

$$\begin{aligned} \Gamma_{II,\mathbf{S}',Z';l,k} = {} & \frac{2m}{\hbar^3} N_I \left(\frac{Z_I e^2}{4\pi\epsilon} \right)^2 \frac{1}{(2\pi)^3} \\ & \times \sum_{j=1}^{2} \frac{1}{2|q_j + k|} \sum_{l'} \left| \int d\mathbf{q}_S \int \frac{4\pi d\mathbf{s} v \xi^*_{l'}(\mathbf{s}) \xi_l(\mathbf{s}) e^{i\mathbf{q}_S \mathbf{s}}}{\mathbf{q}_S^2 + q_j^2 + (1/L_D)^2} \right|^2. \end{aligned} \tag{A11}$$

In this case, $q_{1,2}$ are the same as in equation (A2).

A.4. Surface roughness scattering rate derivation

Assuming that x is the direction of transport along the nanowire, we describe the variations of the surface of the wire by defining the quantities

$$\Delta(y) = S(y) - F(y) \qquad \text{and} \qquad \Delta(z) = S(z) - F(z), \tag{A12}$$

where S is the border line of the ideal surface and F is a legitimate border line between the wire and the environment. The perturbation Hamiltonian can be written as

$$H' = e\mathbf{E}_y(\mathbf{s}, x)\Delta_y(x) + e\mathbf{E}_z(\mathbf{s}, x)\Delta_z(x), \tag{A13}$$

where $\mathbf{E}_y$ and $\mathbf{E}_z$ are the electric field component in the cross section normal to the direction of transport. The final scattering rate can be expressed as [27]

$$\Gamma_{SR,l,k} = \sum_{l'} \frac{e^2}{\hbar}|N_{\mathrm{E}}(l, l')|^2 D^2 \frac{m}{\hbar^2} F(k)\theta(\epsilon_f), \tag{A14}$$

where

$$F(k) = \left(\frac{2\sqrt{2}\,\lambda}{(2 + \lambda^2(k - k_1')^2)} \frac{1}{|k_1'|} + \frac{2\sqrt{2}\,\lambda}{(2 + \lambda^2(k - k_2')^2)} \frac{1}{|k_2'|} \right) \tag{A15}$$

and

$$N_{\mathrm{E}}(l, l') = N_{\mathbf{E}_{y,z}}(l, l') = \int d\mathbf{s}\xi_{l'}^*(\mathbf{s})\mathbf{E}_{y,z}(\mathbf{s}).\xi_l(\mathbf{s}). \tag{A16}$$

Here, the θ function comes from the requirement for the existence of the square root

$$k_{1,2}' = \pm\sqrt{\frac{2m}{\hbar^2}(E_l + \epsilon(k) - E_{l'})} = \pm\sqrt{\frac{2m}{\hbar^2}\epsilon_f}\,. \tag{A17}$$

The result is generalized for the particular y and z components. Also, D is the root mean square of the variance of Δ and λ is the correlation length.

ORCID iDs

Cristina Medina-Bailon https://orcid.org/0000-0002-4280-3149
Siegfried Selberherr https://orcid.org/0000-0002-5583-6177

References

[1] Ionescu A M and Riel H 2011 *Nature* **479** 329–37
[2] Björk M T, Knoch J, Schmid H, Riel H and Riess W 2008 *Appl. Phys. Lett.* **92** 193504
[3] Imenabadi R M, Saremi M and Vandenberghe W G 2017 *IEEE Trans. Electron Devices* **64** 4752–8
[4] Saremi M, Afzali-Kusha A and Mohammadi S 2012 *Microelectron. Eng.* **95** 74–82
[5] Sadi T, Towie E, Nedjalkov M, Riddet C, Alexander C, Wang L, Georgiev V, Brown A, Millar C and Asenov A 2016 One-dimensional multi-subband Monte Carlo simulation of charge transport in si nanowire transistors *In Proc. Int. Conf. Simulation Semiconductor Processes Devices (SISPAD) (Nuremberg, Germany, 06-08 September 2016)* (IEEE) pp 23–6
[6] Li Y and Hwang C H 2009 *Semicond. Sci. Technol.* **24** 095018
[7] Zhang L, Li L, He J and Chan M 2011 *IEEE Electron Device Lett.* **32** 1188–90
[8] Kumar S and Jha S 2013 *Microelectron. J.* **44** 844–51
[9] Al-Ameri T, Georgiev V P, Sadi T, Wang Y, Adamu-Lema F, Wang X, Amoroso S M, Towie E, Brown A and Asenov A 2017 *Solid-State Electron.* **129** 73–80
[10] Sadi T, Medina-Bailon C, Nedjalkov M, Lee J, Badami O, Berrada S, Carrillo-Nunez H, Georgiev V, Selberherr S and Asenov A 2019 *Materials* **12** 124
[11] Medina-Bailon C, Sadi T, Nedjalkov M, Carrillo-Nuñez H, Lee J, Badami O, Georgiev V, Selberherr S and Asenov A 2019 *IEEE Electron Device Lett.* **40** 1571–4
[12] Jin S, Tang T W and Fischetti M V 2008 *IEEE Trans. Electron Devices* **55** 727–36
[13] Esseni D, Palestri P and Selmi L 2011 *Nanoscale MOS Transistors: Semi-Classical Transport and Applications* (Cambridge: Cambridge University Press)
[14] Tienda-Luna I M, Ruiz F G, Godoy A, Biel B and Gámiz F 2011 *J. Appl. Phys.* **110** 084514
[15] Zhang W, Delerue C, Niquet Y M, Allan G and Wang E 2010 *Phys. Rev.*B **82** 115319
[16] Niquet Y M, Delerue C, Rideau D and Videau B 2012 *IEEE Trans. Elec. Devices* **59** 1480–7
[17] Niquet Y M, Delerue C and Krzeminski C 2012 *Nano Lett.* **12** 3545–50
[18] Ferry D and Jacoboni C (ed) 1992 *Quantum Transport in Semiconductors* (US: Springer)
[19] Badami O, Medina-Bailon C, Berrada S, Carrillo-Nunez H, Lee J, Georgiev V and Asenov A 2019 *Appl. Sci.* **9** 1895
[20] QuantumATK Version O-2018.06, Mountain View, CA, USA, Jun. 2018
[21] Garand User Guide O-2018.06, Mountain View, CA, USA, Jun. 2018
[22] Gnani E, Reggiani S, Gnudi A, Parruccini P, Colle R, Rudan M and Baccarani G 2007 *IEEE Trans. Elec. Devices* **54** 2243–54
[23] Wang J, Rahman A, Ghosh A, Klimeck G and Lundstrom M 2005 *IEEE Trans. Elec. Devices* **52** 1589–95
[24] Esseni D and Driussi F 2011 *IEEE Trans. Elec. Devices* **58** 2415–22
[25] Neophytou N and Kosina H 2011 *Phys. Rev.*B **84** 085313
[26] Jin S, Fischetti M V and Tang T W 2007 *J. Appl. Physics* **102** 083715
[27] Ramayya E B, Vasileska D, Goodnick S M and Knezevic I 2008 *J. Appl. Physics* **104** 063711
[28] Jacoboni C and Reggiani L 1983 *Rev. Mod. Phys.* **55** 645–705